Journal of Photochemistry and Photobiology 20 (2024) 100231

Contents lists available at ScienceDirect

Journal of Photochemistry and Photobiology

journal homepage: www.sciencedirect.com/journal/journal-of-photochemistry-and-photobiology

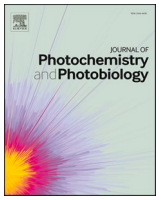

Fenton-mediated solar-driven photocatalysis of industrial dye effluent with polyaniline impregnated with activated TiO_2-Nps

Joshua Akinropo Oyetade *, Revocatus Lazaro Machunda, Askwar Hilonga

School of Materials, Energy, Water and Environmental Sciences, Nelson Mandela African Institution of Science and Technology P.O. Box 447, Arusha, Tanzania

ARTICLE INFO

Keywords:
Photodegradation
Photocatalysis
Photons
Composites
Effluent

ABSTRACT

Various integrated technologies have been investigated for the remediation of heavily polluted industrial dye effluent. Also, more than 70 % of these dyes are known to be solely azo dyes used in the textile industry with 5–30 % presence in the effluent as loose dye molecules which are recalcitrant to treatment. These challenges led to the investigation of energy-efficient processes (solar) and the fabrication of high-performance nano-photocatalysts for proficient photocatalysis of dye effluent while mediating the process with Fenton reagents. The study fabricated nanopolymeric catalyst composites (P-AKT) via novel in situ coupling and impregnation of the polyaniline (PANI) with surface-activated TiO_2 NPs. This fabrication is aimed at developing a high-performance catalyst with rapid and proficient photocatalytic activities to photons from sunlight irradiation. The photocatalytic process was mediated using a novel Fenton reagent to enhance the generation of radical species for dye degradation. Various instrumental characterization methods were used to study the structural, molecular, elemental, functional and optoelectronic properties of the fabricated nanocomposite photocatalysts. The result reveals functional groups aiding dye-catalyst bonding and morphological interaction reveal a surface-activated tetragonal crystalline mixture of anatase and rutile from TiO_2Nps embedded in the macromolecular chain of PANI. It also reveals the optimal conditions of 20 mg dosage, 10 mg/L initial concentration with substantial effectiveness at pH of 5 and 7. However, the most efficient photocatalyst recorded was P-AKT-2 % and P-AKT-3 % having 95 % and 94 % efficiencies at 90 min of solar irradiation. The photocatalyst equally demonstrated its capacity for effluent treatability up to 4 cycles of use.

1. Introduction

Textile industries are saddled with various unit processes for textile apparel. These are generally classified as either wet or dry treatment processes [1,2]. However, the wet treatment processes of textile operations such as printing, dyeing and pigmentation are associated with a large volume of effluent heavily polluted with loose dyestuff [3–5]. The effluent resulting from these textile industries mostly consists of synthetic industrial dyes associated with significant genotoxic impacts on flora, fauna, man and the environment at large [6,7]. Among the commonly used industrial dyes are the synthetic azo dyes. These dyes are characterized by recalcitrant and chemo-transformative properties in effluent which often impart deleterious effects on land and in water bodies [8–10]. However, the emphasis on these highly valued azo dyes is based on vital properties such as excellent fastness rating on the textile substrate, formation of brilliant hues and cost-effective synthetic route [11,12]. However, their presence in wastewater as effluent commonly undergoes the cleavage of the azo group transforming into aromatic compounds with acute carcinogenic effects [7,13,14].

Although, various conventional treatment has been adopted for effective clean-up of textile effluent before discharge especially the recent use of advanced polymeric nanocomposite membranes for water and industrial effluent treatment [15]. Studies also address the use of state-of-the-art fabricated nanocomposites like cellulose graft copolymers and magnetic Fe_3O4/Polypyrrole/Carbon Black nanocomposite for the treatability of dye effluent via adsorption process [16,17]. However, challenges such as the difficulties in the separation of the dye molecules after adsorption from aqueous media, the resistance of these dyes to other forms of treatment techniques, energy and cost intensiveness remain major challenges. Also, most of these technologies merely transfer these recalcitrant dye molecules from one phase to another leaving toxic sludge characterized by secondary pollutants [18–20]. This necessitates the need for the investigation of the photocatalytic technique which plays a premium role in the complete

* Corresponding author.
E-mail addresses: joshuaoyetade@gmail.com, oyetadej@nm-aist.ac.tz (J.A. Oyetade).

https://doi.org/10.1016/j.jpap.2024.100231

Available online 7 February 2024

degradation of these recalcitrant dye molecules. The process involves the use of photocatalysts with an appreciable bandgap that can initiate the generation of hydroxyl, superoxide radicals that will react with the dye molecules leading to their mineralization into water and CO_2 [18,21]. Although, various catalyst has been studied ranging from the semiconductors such as TiO_2, Cu_2O, ZnO, H-BN, Graphene Oxide, Al_2O_3, Fe_2O_3, FeO, WnO_2 and SnO_2 to various polymeric materials [22,23]. However, the quest for band gap tunability to enhance its sensitivity to visible light, reduction in agglomeration of the particles, availability of sufficient radicals for rapid dye degradation, immobilization of the catalyst to avoid leaching and proficient electron transport dynamics led to the recent investigation of composite formation [21]. This involves the coupling or impregnation of the novel conducting polymers with semi-conductors, especially TiO_2 which stands out with excellent oxidizing attributes among others [24].

Among the investigated conducting polymers, polyaniline (PANI), polyaniline stands out with unique electron mobility, thermal and chemical stability. It has appreciable surface functional properties and effective synergism with semiconductor materials via in-situ or ex-situ polymerization. Coupling of semiconductors with this polymer forms a versatile nano polymeric composite photocatalysts [24,25]. Also, one of the most pivotal reasons for coupling conducting polyaniline with semiconductor photocatalysts is based on the optoelectronic impacts of PANI in the mix [26]. However, reported limitations such as longer irradiation time required for solar-driven photocatalysis and ease in catalyst deactivation due to leaching and agglomeration remain. Also, the need for green energy applications to drive the process efficiently in contrast with commonly used UV irradiation led to this study [7,27]. The novelty of this study is expressed in the development of high-performance solar-driven photocatalyst nanocomposites with rapid degradation activity for the recalcitrant dye molecules. In addition, the study seeks to incorporate a novel electro-Fenton mediation process for the generation of sufficient free radicals. The process involves the study of the combing possibility of ferrous ion which has proficient activity with hydrogen peroxide as an oxidant under solar irradiation. this generates Fe^{2+} which combines as an active oxidant with the hydroxide radicals from H_2O_2. The radicals species combine with the radicals generated on the surface of the fabricated photocatalyst to enhance rapid dye degradation [28]. The collaboration of these radicals with those generated by the irradiated photocatalyst will trigger unique spontaneity in dye degradation under solar photon irradiation. Thus, the current study seeks to incorporate novel Fenton reagents to mediate the solar photocatalytic process of the model dye (methylene blue) using nano photocatalyst composites fabricated from polyaniline impregnated with surface activated TiO_2—Nps.

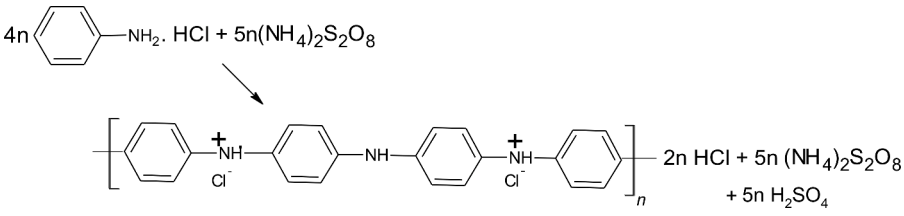

(1)

2. Materials and methods

2.1. Materials

The aniline used ($C_6H_5NH_2$: LOBA, 99 %) was double distilled and stored in a dark bottle before its use. Also, TiO_2 (P25) with a purity grade of 99.5 %, ammonium peroxydisulfate (99 %), HCl (37 % v/v), NaOH, anhydrous $FeCl_3$ and Methylene blue dye ($C_{16}H_{18}ClN_3S$) were purchased from LOBA chemical industries, India while H_2O_2 (30% $_{V/V}$) was purchased from Sigma and Aldrich, USA. De-ionized water was also used throughout the experiment, while glassware and equipment such as an oven, analytical weighing scale, and centrifuge, sonicator, UNICO 2800 UV–VIS spectrophotometer and solar power meter (Datalogging-TES 132) were procured at the Nelson Mandela African Institution of Science and Technology (NM-AIST), Tanzania.

2.2. Preparation of activated titanium oxide NPS (AKT-NPs)

Alkali-activated titanium nanoparticles (AKT-NPs) were prepared via the modified method of Hou et al. [24] and Sharma et al. [25]. This involved weighing 1.5 g of TiO_2 into 100 mL of 3 M NaOH with stirring for 3 hrs, then left undisturbed for 2 hrs. The mixture was then centrifuged at 3000 rpm, filtered and washed three times with ultrapure water before drying for two hours at 105 °C in the oven. The resulting material was calcinated at 450 °C for 2 hrs to eliminate water trappings and to enhance its surface activation for effective synergism with other materials. The solid sample was then pulverized to obtain powdered material and labeled as (AKT-3 %).

2.3. Synthesis of polyaniline (PANI)

The synthesis of the macromolecule (PANI) was carried out via the oxidative polymerization method. The reaction involves the use of 0.0215 mol double distilled aniline in 30 ml of 1 M $HCl_{(aq)}$ with dropwise addition of 0.0215 mol ammonium persulfate (APS) as an oxidant, described in Eq. (1) [22,23]. The set-up was carried out in an ice bath of 0–5 °C with uniform stirring for 4 hrs and kept in the refrigerator at 4 °C overnight. The precipitated green polyaniline emeraldine was washed with 0.5 M HCl, filtered then re-washed with deionized water to obtain neutral filtrate. The residue was further washed with a mixture of acetone and ethanol (1:1) to remove the remaining monomers and oligomers before vacuum drying at 80 °C for 2 hrs.

2.4. Fabrication of polyaniline impregnated with activated Tio_2 Nps

The fabrication of nanocomposite via the impregnation of alkali-activated TiO_2—Nps was carried out via in situ impregnation using the modified method of Lee et al. [27] and Shahabuddin et al. [20]. The processing involves the dispersion of 1 % activated TiO_2 Nps already sonicated in 5 ml ultrapure water. The dispersoid was added dropwise to 0.0215 mol of aniline in HCl with constant stirring, before the dropwise addition of equal mole of ammonium persulfate (APS). The mixture was stirred for 6 h in an ice bath (Fig. 1). And then kept in the refrigerator at 4 °C overnight. The polymerized precipitate was filtered, washed with DI, ethanol, methanol: acetone and dried at 75 °C for 12 h and labeled P-AKT-1 %. Similar reaction was carried using 2 %, 3 %, 4 % and 5 %

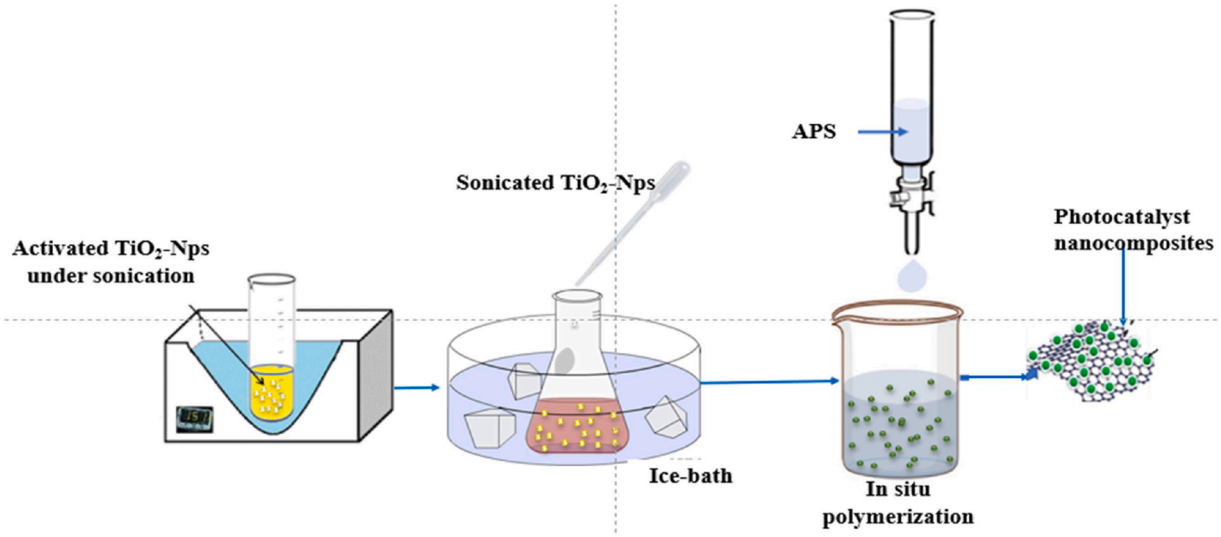

Fig. 1. Fabrication of nanopolymeric photocatalyst nanocomposites.

activated TiO_2—Nps impregnation and was labelled as P-AKT-2 %, P-AKT-3 %, P-AKT-4 % and P-AKT-5 %.

2.5. Instrumental characterization

The surface morphology and elemental constituents of the fabricated nano photocatalyst were analyzed using a JEOL JSM-7600F field emission scanning electron microscope functioning at 10 kV. The EDX was used to access the elemental composition, while the internal structural properties such as the size, shape and crystallinity of the materials under investigation were studied using JEOL JEM-2100F high-resolution transmission electron microscope. The crystalline structure of the materials was investigated using a Rigaku Ultima IV X-ray diffractometer (XRD) with Cu Kα radiation (k= 1.5418 A) at a scanning rate of 0.02 s^{-1}. The functional group features of the nanomaterials were recorded on a QATR-Shimazu Infrared spectrometer (Japan) in a range from 4000 to 400 cm^{-1}. Brunauer–Emmett–Teller (BET) system (NOVA2200e) and Barrett–Joyner–Halenda (BJH) desorption isotherms were used to analyze the pore structures and the corresponding specific surface areas. Also, the wave scan of the respective photocatalyst was analyzed using UNICO 2800 UV–VIS spectrophotometer (Thermo Scientific) their respective band gap was determined using Tauc expression in Eq. (2)

$$(\alpha.\ h\upsilon)^{1/n} = B\left(h\upsilon - E_g\right) \tag{2}$$

where the Plank's constant is h, υ represents the photon frequency, Eg indicates the band gap energy (eV), B is a constant, n represents a dependent factor which is a function of electron transition property and the absorbance coefficient is represented by α.

2.6. Measurement of photocatalytic activities with incident solar radiance

The photocatalytic activities of the fabricated photocatalyst nanocomposites were investigated through the use of the model dye (methylene blue) under the intensity of solar irradiation for electron excitation [29]. The set-up involves the use of varying percentages of nano photocatalyst composites fabricated P-AKT (1,2,3,4,5 wt%) for the photocatalytic degradation of 100 mL known concentration of methylene blue. This effluent was initially subjected to a dark room for adsorption-desorption equilibrium for 60 min [20,30]. Then the study of the photo-degradation of the dye pollutant was executed on sunny days, from March to May where the sun intensity is highest in Arusha (3° 23′ 59″ S and longitude 36° 47′ 47″ E between 11:30 am-2:30 pm). The pyranometer (Datalogging-TES 132) was used to measure the sunlight radiance by tilting the sensor of the device to the point of highest sunlight intensity (solar zenith angle) [29,31]. The degradation rate was quantified using UNICO 2800 UV–VIS spectrophotometer (Thermo Scientific) at the predetermined wavelength of 663 nm before sunlight exposure (control) (C_0) and after irradiation with sunlight (C_t) respectively. The degradation efficiency was calculated using the formula in Eq. (3) while the quantity adsorbed at equilibrium (Q_e) and at time t (Q_t) was determined via the formula in Eqs. (4) and (5).

$$\%\text{Degradation Efficiency} = \frac{C_t - C_0}{C_0}\ X\ 100 \tag{3}$$

$$\text{Quantity adsorbed at Equilibrium (Qe)} = \frac{(C_0 - C_e)\ X\ V}{m} \tag{4}$$

$$\text{Quantity adsorbed at Equilibrium (Qt)} = \frac{(C_0 - C_t)\ X\ V}{m} \tag{5}$$

3. Results and discussion

3.1. Morphological assessment of fabricated nanocomposites

The results in Fig. 2(a-g) show the SEM image of polyaniline (PANI), the alkali surface activated TiO_2—NPs (AKT-3 %) and the fabricated nanocomposites P-AKT (1–5 %) respectively while Fig. 2(h)-(i) shows the XRD spectra for PANI and AKT-3 % respectively. Similarly, Fig. 3(a) shows the internal structural features of the selected fabricated photocatalysts nanocomposites (P-AKT-3 %) via HR-TEM imaging, and Fig. 3 (b) reveals the SAED pattern of the photocatalyst. The XRD pattern of the fabricated composites (P-AKT-1 to 5 %) was also depicted in Fig 3(c) while Fig. 3(d), (e) and (f) show the 3D surface imaging of PANI, Activated TiO_2—Nps and the corresponding fabricated photocatalyst composites. From the SEM imaging results of PANI, there was an evident rod-like polymeric network observed which is related to the densely interconnected polymeric networks of PANI [7,32,33]. Also, the morphological analysis via SEM for the activated TiO_2 Nps in Fig 1(b-b^1) is in tandem with the image of TiO_2 reported by Hou et al. [24] and Zhou et al. [34]. However, with a well-defined nanospheric shape and a higher amount of anatase than rutile constituent from the XRD diffraction peaks in Fig. 2(i). This is because the anatase phase from the pattern has a greater proportion and features more prominently than the rutile phase in the XRD pattern [35]. Phromma et al. [31] further revealed that a lower temperature of <500 °C favours lower crystallite size of TiO_2 which equally reduces the rate of agglomeration and aggregation of the

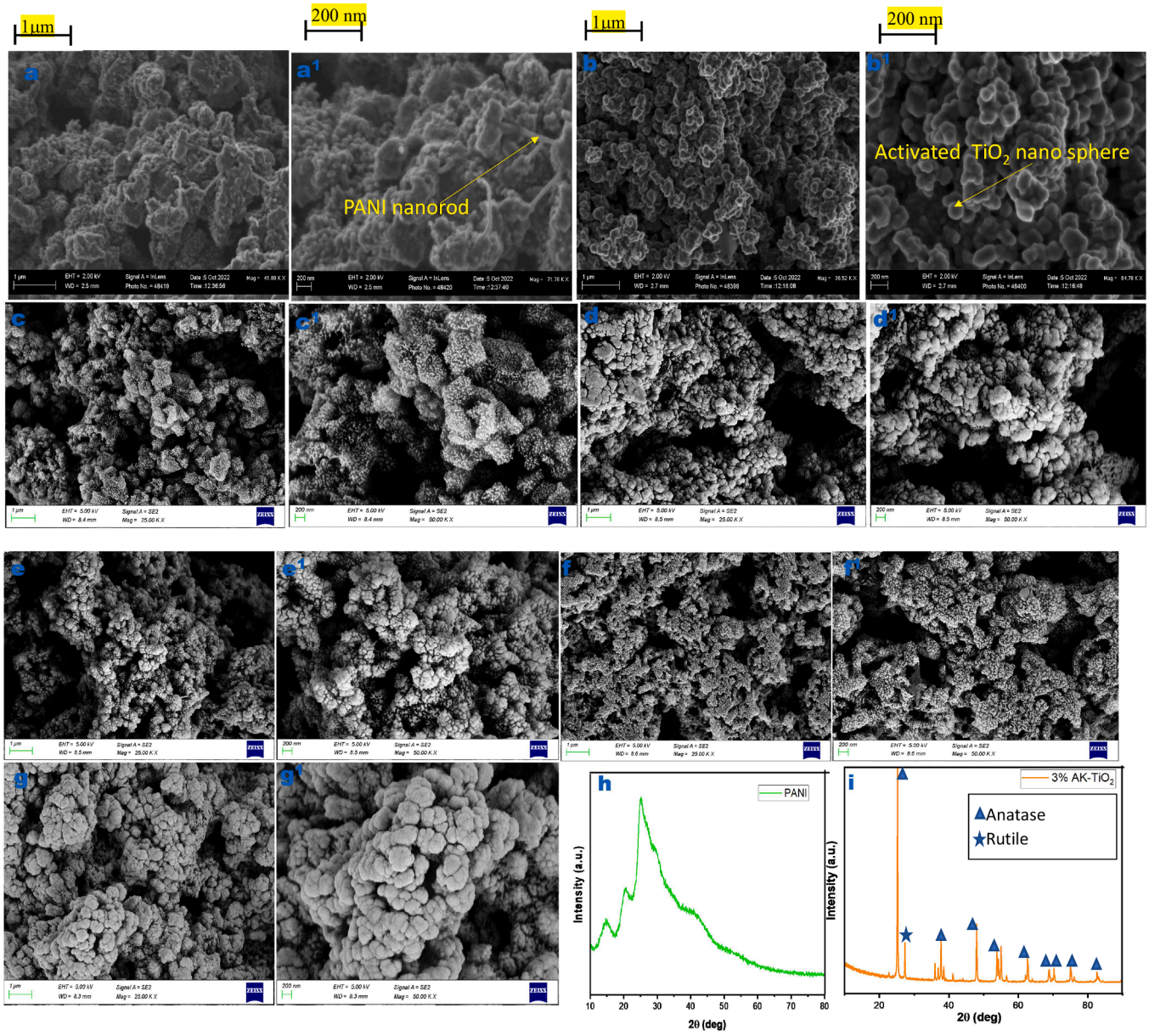

Fig. 2. (a-g) SEM image of PANI (a-a[1]); AKT-3 % (b-b[1]); PAKT-1 % (c-c[1]); PAKT-2 % (d-d[1]); PAKT-3 % (e-e[1]); PAKT-4 % (f-f[1]); PAKT-5 % (g-g[1]); (h) XRD of PANI; (i) XRD spectra of AKT-3 %.

nanoparticles. In addition, Oyetade et al. [36] suggested that the alkali surface activation treatment given to TiO_2 Nps enhances its synergism and surface activity when incorporated as a sonicated suspension to the conducting macromolecules to form photocatalytic composites.

Also, Lu & Astruc [31] and Martakov [32] observed that surface activation for semiconductors like TiO_2 lowers the amount of possible impurities that meddle with desired properties such as bandgap, functional groups and adsorption capacity which precedes effective photocatalysis of dye molecules. The XRD pattern in the figure affirms respective angles such as 25°, 38°, 48°, 55.1° and 63.2° which correspond to (101), (103), (200), (211) and (204) peak planes of anatase--TiO_2, while the spectra equally feature the structural patterns of rutile-TiO_2 at the 110 planes [37]. Similarly, the XRD spectra of conductive macromolecule (PANI) indicate characteristic peaks at 2θ =15.78 ^{0}, 20.45 ^{0}, and 25.35 ^{0}. The XRD pattern of PANI reflects amorphous properties of the conductive macromolecules based on the repetition of benzenoid and quinoid rings along PANI chain [38,39]. A similar observation in the diffraction patterns indicated by the peaks was reported by Habtamu et al. [33] and Shahabuddin et al. [20]. Shahabuddin et al. [20] affirmed that the diffraction pattern of PANI with the sharp peaks at 2θ = 20.35 and 25.25 is attributed to the periodic repeating of the quinoid and benzenoid rings along PANI chains. However, the spectra generally indicate a high degree of amorphous behavior of PANI which is in contrast with the well-defined crystalline pattern of the activated metal oxide semiconductor (AK-TiO_2—NPs). However, the XRD spectra result after nanocomposites fabrication at various wt/wt% loading of activated TiO_2- Nps in Fig. 3(c) indicate the surface transformation of the peak from well-defined crystalline peak pattern in Fig. 2(i) to amorphous structure with lower peak intensity when the metal oxide is incorporated in situ to polyaniline. This suggests the surface interaction of amorphous PANI in Fig 2(h) with the well-ordered morphology of AK-TiO_2Np resulting in the formation of nanocomposites with a lowered degree of crystallinity as revealed in Fig 3(c). These observed morphological tunability effects of PANI were equally reported by Shahabuddin et al. [20] on 2D-hexagonal boron nitride, TiO_2/Nb_2O5/Reduced graphene oxide by Zarrin &

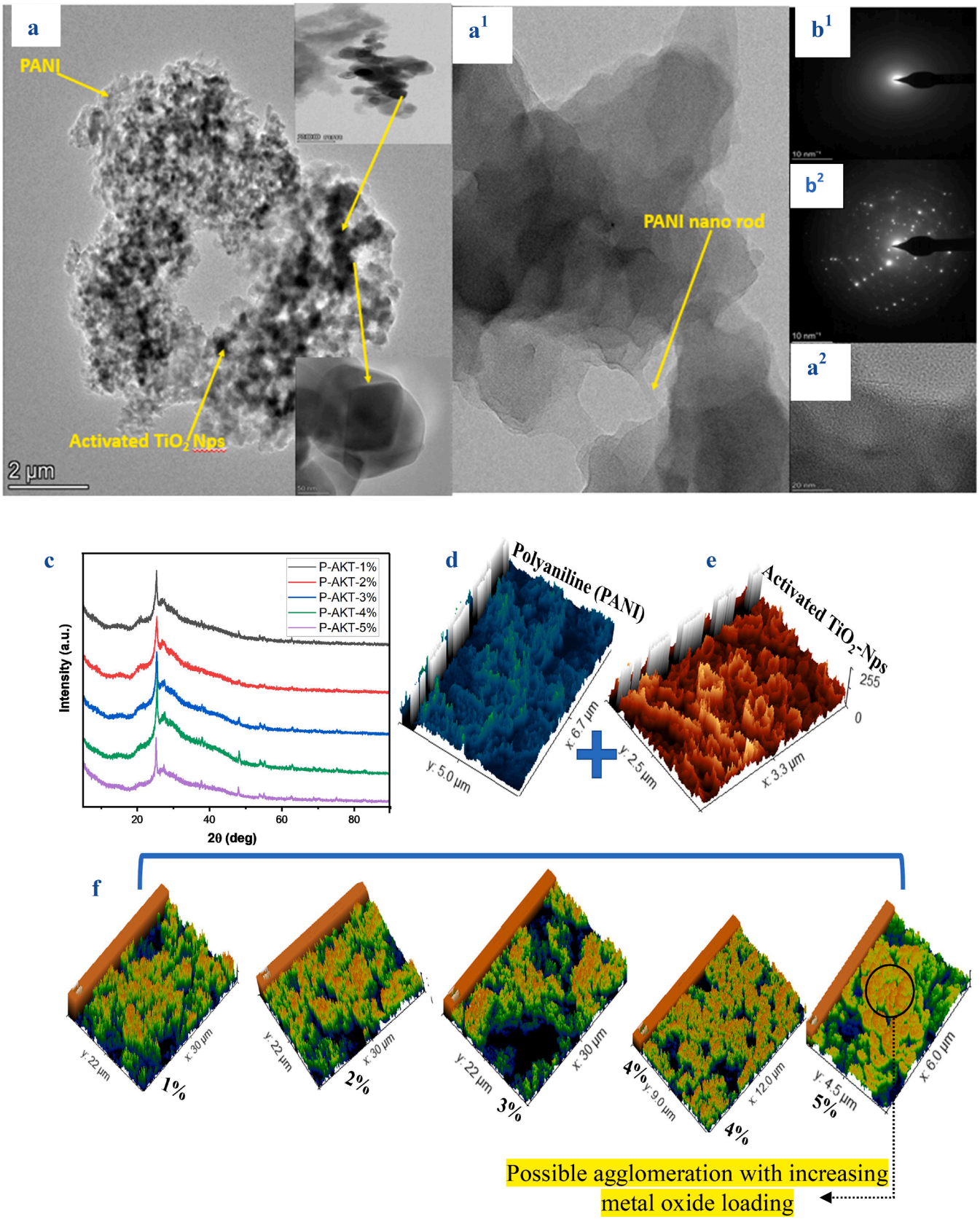

Fig. 3. (a-a^2) HR-TEM of P-AKT-3 % (b) SAED pattern for P-AKT-3 % (c) XRD pattern of P-AKT-1 to 5 % (d) 3D surface imaging of PANI and (e) Activated TiO_2 Nps; (f) Composites P-AKT-1 %; 2 %; 3 %; 4 %; 5 %.

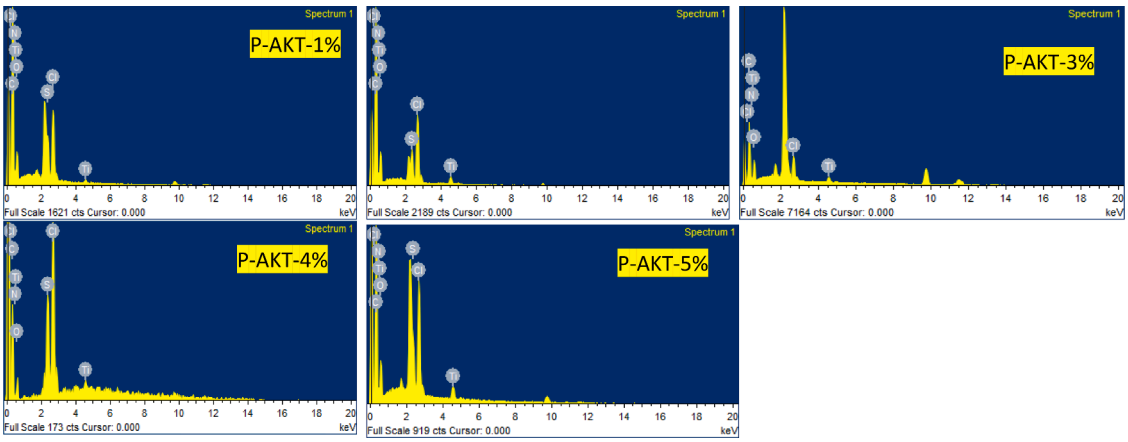

Fig. 4. EDX Spectra of the composites at varying weight percent.

Heshmatpour [40] and TiO_2/reduced graphene oxide by Ma et al. [41]. This action could enhance the availability of active sites on the photocatalyst needed for dye photocatalysis.

Furthermore, the 3D image revealed the surface topology of the fabricated nanocomposites which maintain a similar topology of PANI despite the incorporation of the activated metal oxide Nps at varying wt/wt%. This indicates the domination of the amorphous pattern of PANI over the incorporated crystalline TiO_2—Nps as equally observed by Shahabuddin et al. [23].

However, the 3D image shows the possible formation of an agglomerated surface as the activated metal oxide loading in the polymeric matrix increases. The agglomeration of these nanomaterials often lowers the performance of the photocatalysts in dye photocatalysis after photon irradiation [42,43]. However, the surface tunability impacts of PANI in the blend have the potential of tackling challenges of agglomeration as it creates means of even dispersibility of the catalyst at optimum dosage in the effluent [21]. Furthermore, the TEM result of the fabricated nanocomposites photocatalyst reveals the internal arrangement of the nanocomposites. From the HR-TEM image in Fig 3(a), the result indicates the coating of the conducting polymeric network with the activated TiO_2 Nps which aligns with the SAED pattern Fig. 3(b^1) and (b^2). The selected area electron diffraction (SAED) pattern shows a dominating halo ring pattern which is a characteristic associated with the amorphous material (PANI), unlike the consecutive continuous rings pattern associated with a pattern of polycrystalline materials [44,45]. On the other hand, Fig. 3(b^2) indicates the distinct diffraction spot of TiO_2 Nps in the amorphous chain of PANI. Additionally, the internal investigation via HR-TEM shows the structure features of anatase and rutile (tetragonal crystal structure) which overlays and evenly distributes itself macromolecular polymeric nanorod. Thus, from the morphological view, PANI serves as polymeric support to anchor the activated metal oxides [46]. This synergic action is desirable to lower the leaching rate of the catalyst during photocatalyst and improve the surface activities by lowering the rate of agglomeration apart from improving the dye-catalyst interaction which is a major prerequisite to photocatalysis [21].

3.2. EDX elemental composition

Fig. 4 and Table 1 depict the elemental compositions of the

Table 2
BET surface area analysis.

S/N	Samples	BET Surface area ($m^3\ g^{-1}$)	Pore volume (cm^3/g)
1	P-AKT-1 %	9.449	0.0163
2	P-AKT-2 %	11.317	0.0195
3	P-AKT-3 %	14.671	0.0163
4	P-AKT-4 %	14.320	0.0141
5	P-AKT-5 %	14.320	0.0141

Table 1
EDX elemental composition.

Samples	Elemental composition in wt%					
	C	N	O	S	Ti	Cl
P-AKT-1%	62.44	12.85	14.25	1.74	0.7	8.02
P-AKT-2%	60.83	12.78	15.08	2.03	1.66	7.62
P-AKT-3%	49.35	13.88	29.54	0	2.00	5.32
P-AKT-4%	61.40	8.08	7.91	0	2.39	20.22
P-AKT-5%	68.59	0.98	16.29	0	2.79	11.35

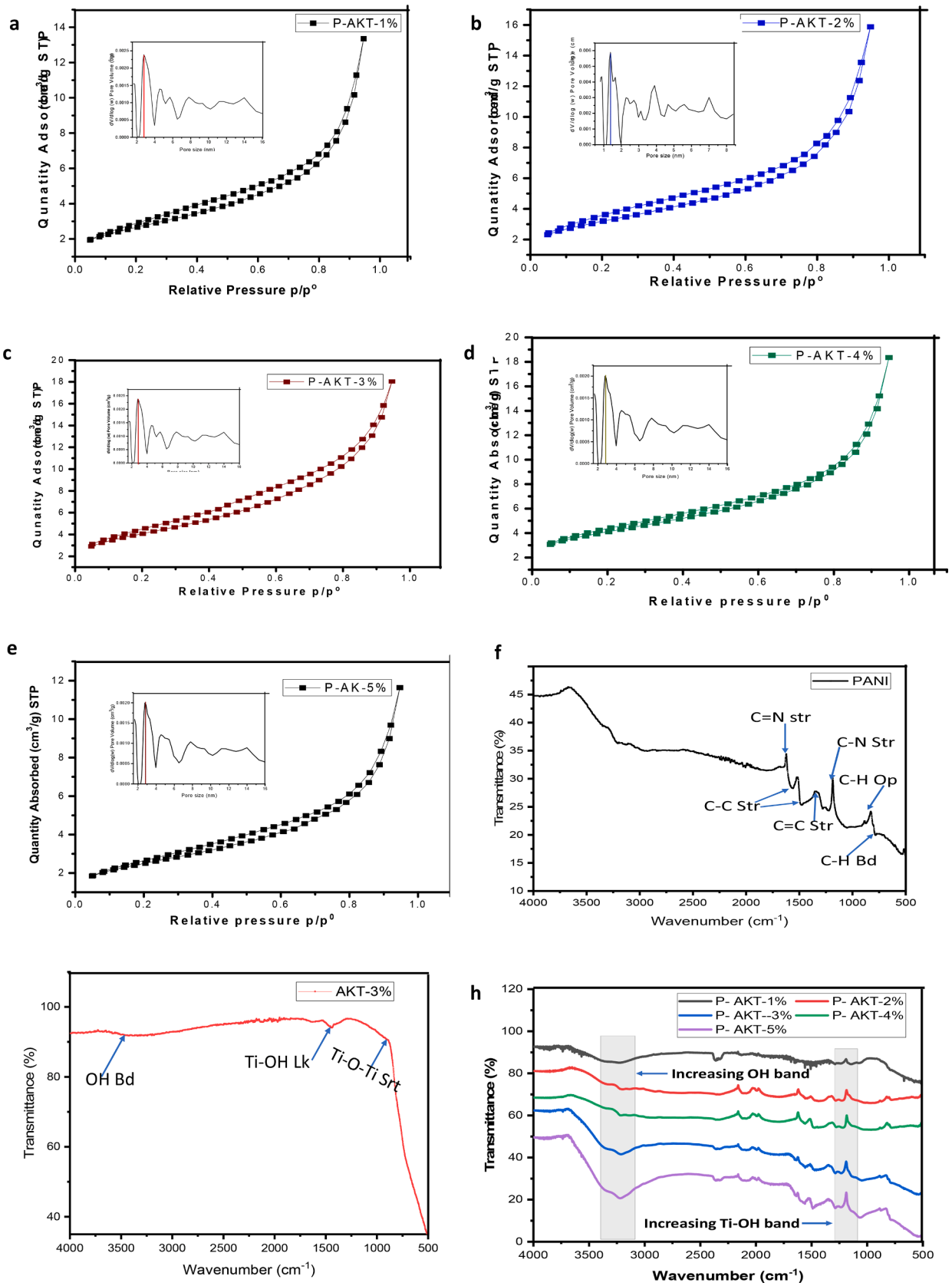

Fig. 5. (a-e) BET adsorption-desorption Isotherm for P-AKT-1 % to P-AKT-5 %; FT-IR Spectra of (f) PANI; (g) Activated TiO_2—Nps; (h) P-AKT-1 % to P-AKT-5 %.

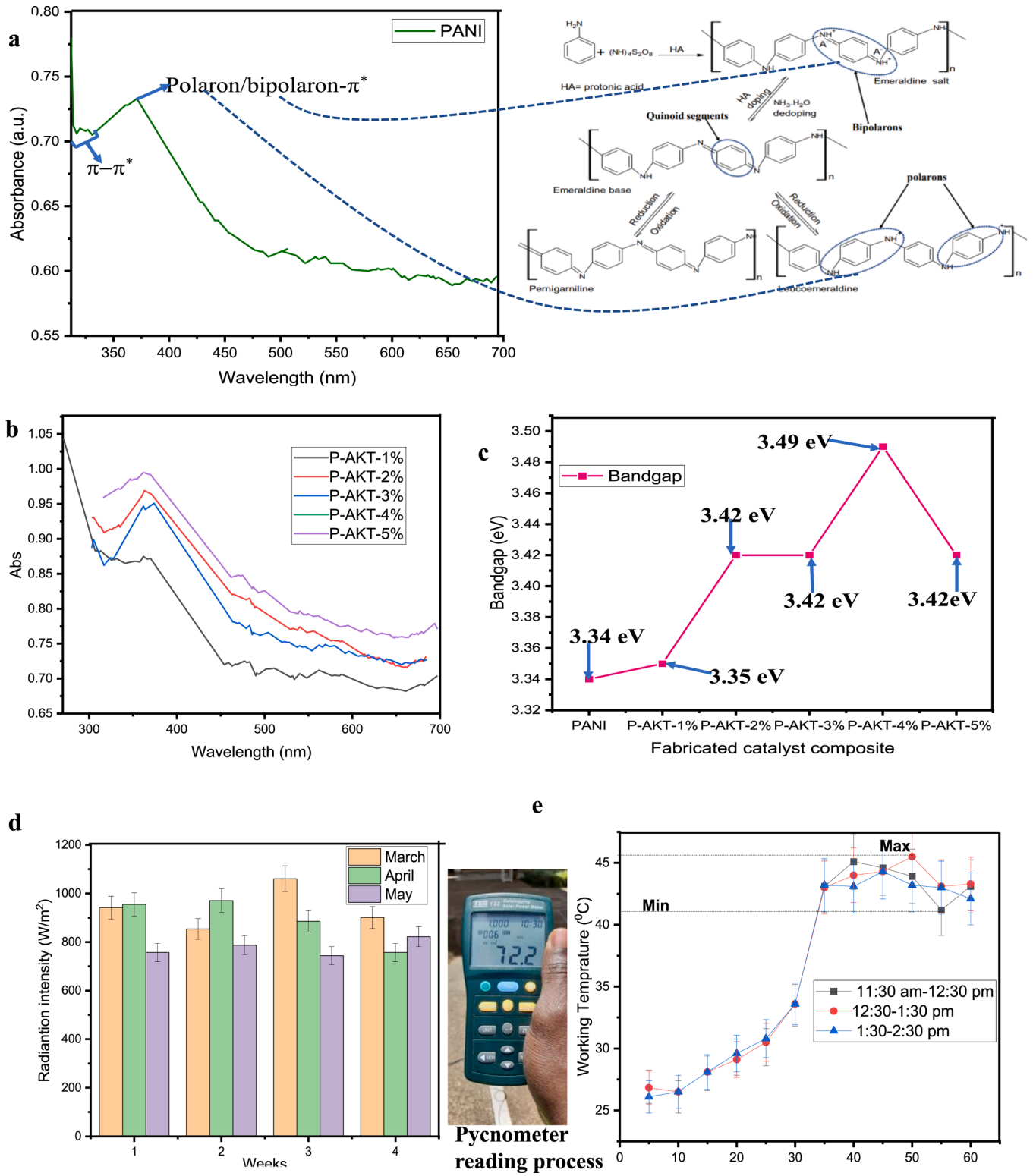

Fig. 6. (a) UV–vis analysis of PANI and (b) P-AKT-1 % to 5 %; (c) bandgap result of photocatalyst; (d) Measurement of solar radiance (e) measurement of working temperature.

fabricated photocatalyst in weight percent (wt%). From the results in Table 1, it is observed that the constituent of Ti increases with increasing addition of wt/wt% of surface-activated TiO_2—Nps. The prevailing elemental composition (C, N, O) in the mix affirms the successful formation of fabricated composite photocatalysts. The presence of these vital elements could improve the availability of active sites for dye-catalyst bonding. The Table also indicated a noticeable increase in the amount of Cl as TiO_2 Nps loading increases. This could be due to either the choice of precursor (titanium isopropoxide and titanium butoxide or titanium tetrachloride) used in the synthesis of TiO_2—Nps or the HCl

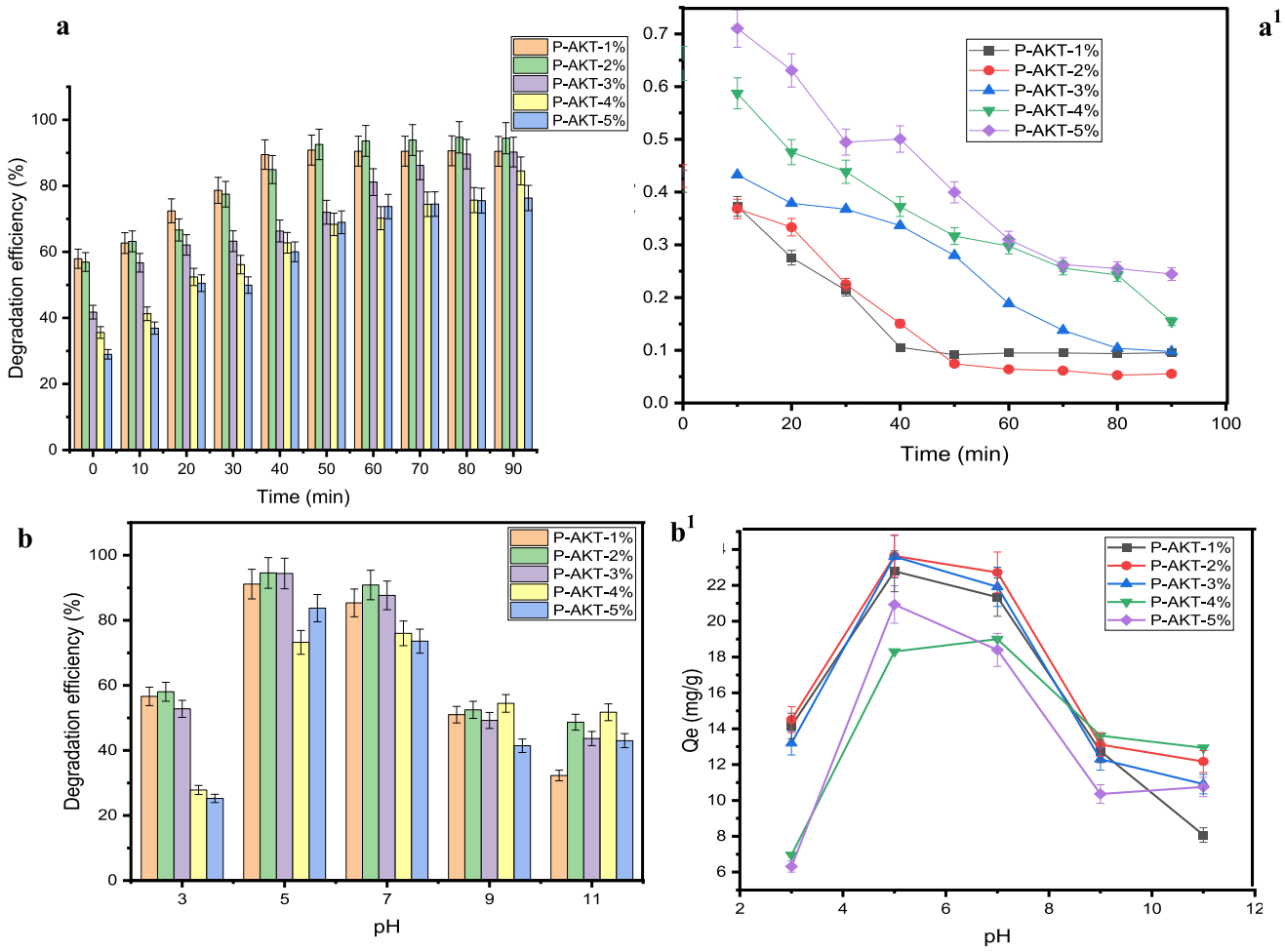

Fig. 7. Effect of time on (a) degradation efficiency; (a^1) Degradation rates; Effect of pH on (b) degradation efficiency; (b^1) quantity absorbed.

used to adjust the pH during the sol formation of TiO_2. This may constitute to the presence of increasing chlorine in the elemental matrix with increasing loading [47,48].

3.3. BET analysis of fabricated photocatalyst

Brunauer-Emmett-Teller (BET) analysis is one of the most effective methods for determining nitrogen adsorption-desorption isotherms. This analysis gives details of the material's surface features such as pore volume, pore size and the hysteresis loop type as seen in Table 2 and Fig. 5(a)-(e). From Table 2, the value of the fabricated composites (P-AKT-1 %) with the lowest surface area and pore volume was 9.449 m^3g^{-1} and 0.0163 cm^3/g respectively, while the highest reported was P-AKT-3 % with a value of 14.671 m^3g^{-1} and 0.0163 cm^3/g for BET surface area and pore volume. Furthermore, it was generally observed for the BET adsorption-desorption Isotherm plot in Fig. 5(a)-(e) was type-IV hysteresis loop a characteristic feature of mesoporous material according to the specified loop pattern by the International Union of Pure and Applied Chemistry (IUPAC) [49–51]. These properties are very crucial in the adsorption process of dye molecules onto the surface of the photocatalysts before the dye mineralization into CO_2 and H_2O. Also, the addition of more activated metal oxide to PANI network increases the surface areas which suggests that doping of PANI with TiO_2 Nps improves the surface area of the conducting polymer which may enhance the availability of more active sites for dye-catalyst interaction [20,21]. Additionally, the observed increase in the surface area of the photocatalysts often enhances proficient and dynamic electron mobility apart from improved ion diffusion thereby increasing the rate of photochemical activities [52–54].

3.4. FT-IR analysis

The FT-IR spectra of the activated metal oxide nanocatalyst (AK-TiO_2 Nps) and polyaniline (PANI) are depicted in Fig. 5(f) and (h). From the spectra, the peak intensity observed around 400–800 cm^{-1} which indicates the functional features of the transition metal (Ti) bonded with a heteroatom (O) forming a Ti-O bond. Also, at 1400 cm^{-1} the stretching vibration ascribed to Ti-O-Ti was observed [55,56]. Similar to the spectra, the observed O—H bend at 3454.51 cm^{-1} is frequently attributed to the hydrogen bond-associated OH free radical. Likewise from the spectra, the bend of O—H observed at 3454.51 cm^{-1} is often assigned to the OH free radical associated with hydrogen bond [57,58]. Furthermore, the FT-IR spectra of PANI in Fig. 5(h) reveal characteristic peaks of C—H bending at 783 cm^{-1}, while the C=N stretching of the PANI nano tubular network was observed at 1685 cm^{-1} and band at 1292 cm^{-1} indicated the C—N stretching. This points to the vibrational interaction of carbon with –NH•$^+$= which accounts for the amphiphilic properties of polyaniline [59]. Also, the spectra display IR peaks at 1563 cm^{-1} and 1482 cm^{-1}, which are attributed to the C=C stretching of the quinoid and benzenoid rings of the PANI homopolymer, respectively. The peaks at 1120 cm^{-1} and 809 cm^{-1} may be attributed to out-of-plane C—H bending in the macromolecular chain [20,25]. On the other hand, the FT-IR spectra result of the fabricated composites from 1 to 5 % wt/wt activated TiO_2 Nps reveals an increasing Ti-OH band as the wt/wt% impregnation with the metal oxide which is equally confirmed by the increasing adsorption band of OH from the spectra [60].

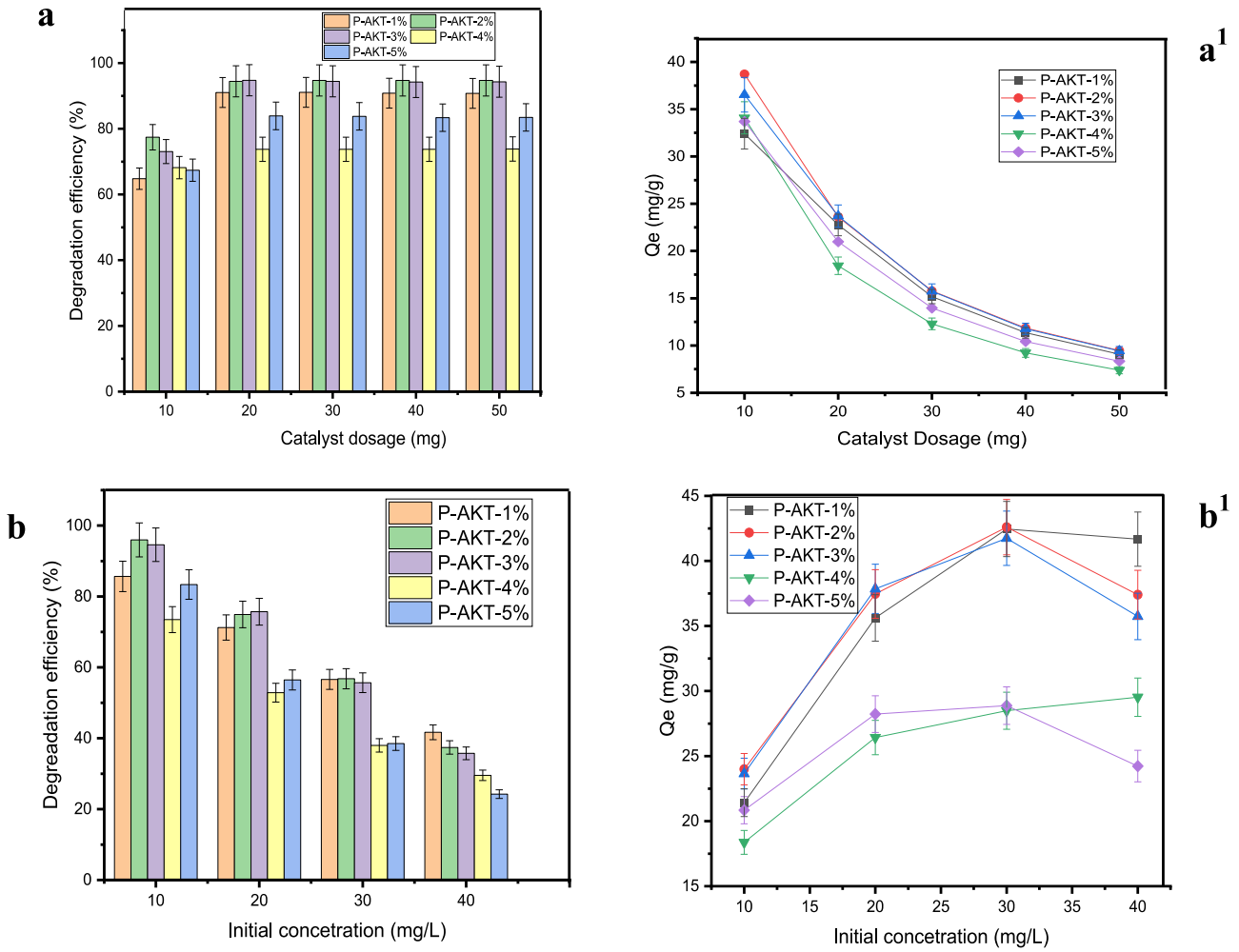

Fig. 8. Effect of dosage on (a) degradation efficiency; (a^1) quantity absorbed; Effect of concentration on (b) degradation efficiency; (b^1) quantity absorbed.

In addition, the functional groups found in pure PANI and activated TiO_2 Nps feature in the fabricated composites. Although the intensities of the functional groups vary, however, the spectra indicate a successful impregnation process. Additionally, the impregnation of the PANI with the activated metal oxide enhances bonding activities such as electrostatic interactions, Van der Waals forces, hydrogen bonding and π–π interactions as a result of multiple functional groups revealed from the FT-IR spectra in Fig. 5(f). The surface functional features observed from these spectra are suggestive of the bond arrangement existing between molecules and the external bonding arrangement that may occur at the surface of the photocatalyst in consonance with the dye molecules in effluent [7,21,45].

3.5. Analysis

The optoelectronic impacts of PANI in the fabricated mix as depicted in Fig 6(a)-(b) via the UV spectra scan of PANI and the corresponding composites at varying wt/wt% impregnation. Also, Fig 6(c) indicates the estimated band gap using fundamental relation (Tauc expression). The maximum wavelength for the UV scan of PANI in Fig 6(a) is at 371 nm which corresponds to the estimated band gap of 3.34 eV in Fig 6(c). However, Majeed et al. [48] pointed out that the optoelectronic characteristics are often associated with their states. This could be leucoemeraldine (completely reduced state), emerald salt (half oxidized state) or pernigraniline (totally oxidized state). However, p-type emeraldine salts exhibit strong exciton bonds and have dynamic charge carrier and electron hopping potential needed during photon irradiation, especially within the visible region [7].

Also, as indicated from the spectra, the synthesized polyaniline positively influences the formation of polarons/bipolarons, thereby supporting the p-type conductivity model. Thus, coupling PANI with activated TiO_2-Nps enhances its optoelectronic activities to solar irradiation which is a major setback for TiO_2. From the result, the increase to 3.49 eV in the bandgap in Fig. 6(c) could be due to the higher addition of the metal oxide semiconductor which results in the reduction of photocatalytic activities. However, the presence of an electronic carrier (polaron) in PANI orchestrates a cation radical of one nitrogen which acts as a hole thereby transferring an elemental positive charge. In addition, the p-type conductivity is achieved when an electron from the nearby nitrogen (neutral) jumps to this hole, making it electrically neutral and starting the motion of the holes through a resonance process [20].

The sensitivity of PANI to photons from solar sources makes the macromolecule act as a photon sensitizers in the blend. Additionally, this macromolecule possesses its own valence and conduction bands called HOMO (Highest Occupied Molecular Orbital) and LUMO (Lowest Unoccupied Molecular Orbital). The HOMO is excited during irradiation thus moving to LUMO via π−π transitions however, often challenged with frequent electron-hole recombination. Interestingly, activated TiO_2 Nps often associated with higher band gap enhance effective charge separation which lowers frequent electron-hole recombination [23].

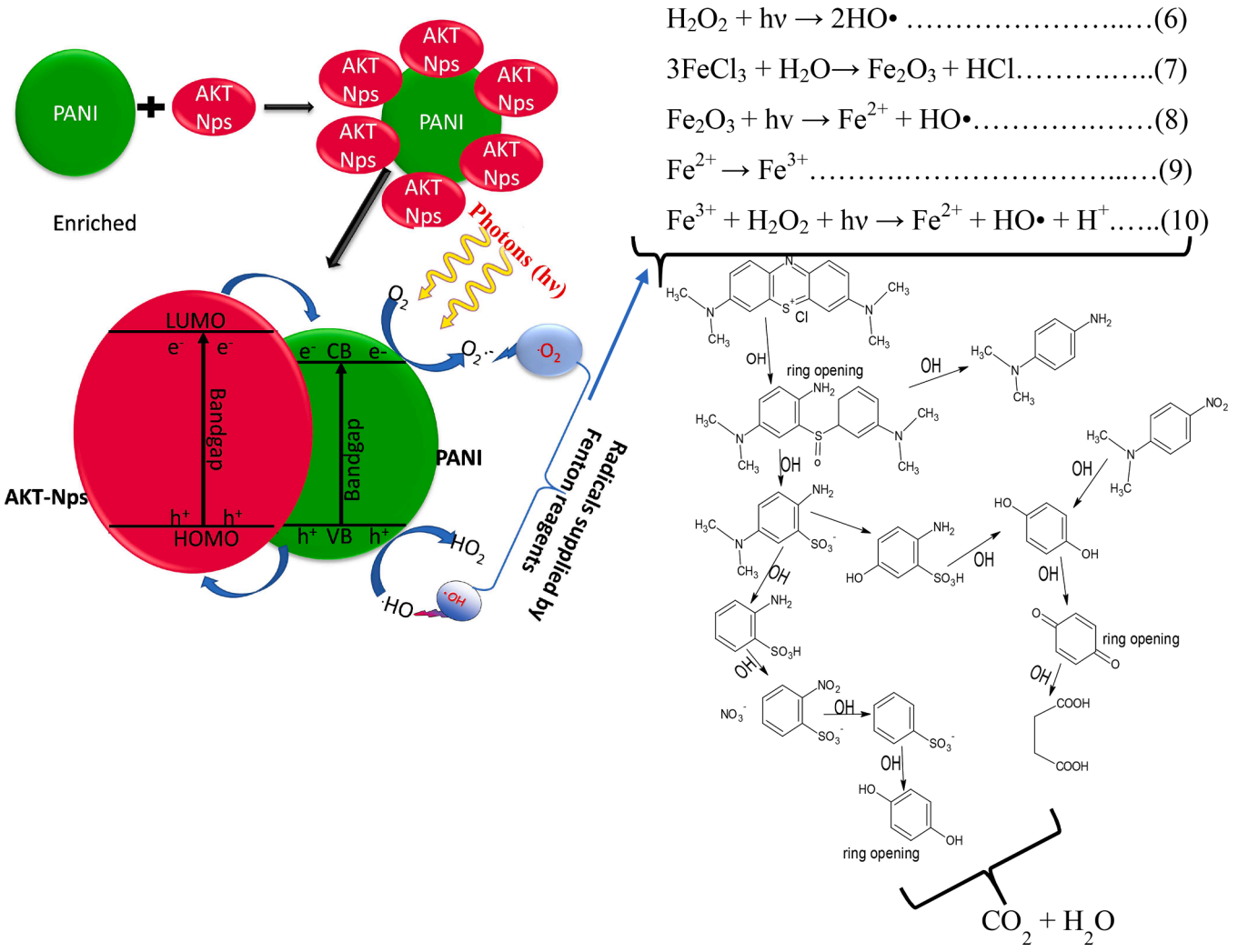

Fig. 9. (a) Regeneration and reuse cycles of P-AKT- and P-AKT-3 % (b) mechanism Composite interaction and synergism.

Table 3
Results of the photocatalytic efficiency of various photocatalysts in comparison.

S/N	Polyaniline based Photocatalyst	Model dye	Conc of dye (mg/L)	Dosage mg/ml	Time (min)	Degradation (%)	References
1	PANI/TiO2/SiO_2 membrane	Methyl orange	1.5	–	90	87	[46]
2	PANI/$SrTiO_3$	Methylene Blue	10.0	0.3	210	95	[76]
3	PANI/ZnO	Methylene Blue	3.2	0.4	300	99	[77]
		Methylene Green			300	97	
4	PANI/TiO_2	Methylene Blue	5.0	1.2	360	99	[78]
			10	10	325.2	91.5	
5	FeO-ZnO/PANI		10	0.2	120	92	[79]
6	Graphene/PANI	Rose Bengal	10	2	180	56	[80]
7	TiO_2/PPy/PANI	Victoria blue	–	–	180	97	[81]
		Rose Bengal			150	97	
8	PANI-Modified TiO2 composite	Methyl orange	–	–	360	21.5 %	[82]
9	PANI/mesoporous silica	Methylene blue	10	2	120	70 %	[83]
10	P-AKT-2 %	Methylene blue	10	0.2	90	95 %	This work
	P-AKT-3 %			0.2	90	94 %	

3.6. Photocatalytic activities

a. Sunlight Radiance and Working Temperature

One of the most prominent factors that constitute to rate and kinetics of the solar-driven photocatalytic process is the intensity of the sunlight radiance and the temperature. The result is depicted in Fig. 6(d) and 6(e) respectively. The results indicate the average weekly solar radiance measured from March to May. From the result, the highest intensity of solar radiance was 1061 W/m^2 in the third week of March while the lowest radiance was at 744 W/m^2 in the second week of May. This implies that the average solar radiance range for the analysis is between 744 and 1061 W/m^2. Similarly, the working environmental temperature measured rose from room temperature to the highest internal 45.5 °C - 41.2 °C in (Fig. 5e). The solar radiance variation is similar to the trend reported by Andrea et al. [49] however, the highest temperature recorded was 48.6 °C. High solar radiance is often accompanied with high-temperature values for the environment and increasing temperature favours the rate of dye photocatalysis [61,62]. Similarly, Kumar and

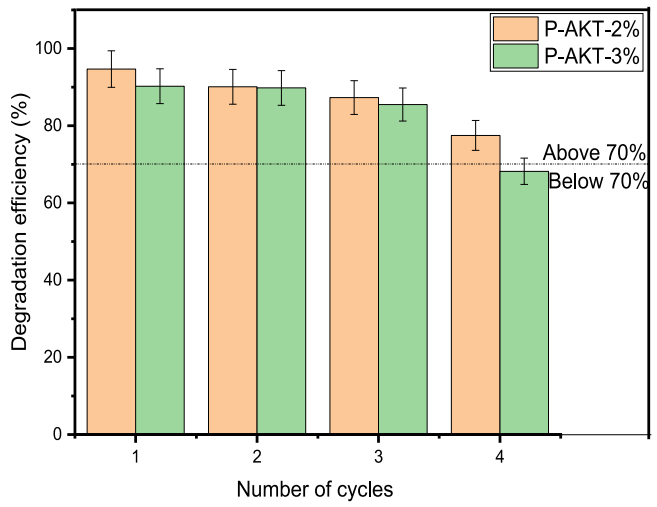

Fig. 10. Reusability cycles of P-AKT-2 % and P-AKT-3 % for methylene blue degradation

Pandey [52] added that the working temperature plays a prime role in the rate of photolysis of organic matter. However, at high temperature (80 °C), the recombination of charge carriers increases which lowers the photocatalytic activities.

b. Effect of Irradiation time

The result in Fig. 7(a)-(a[1]) quantifies the effect of irradiation time at pH 7 and 20 mg/L dosage vis-à-vis degradation efficiency and degradation rates respectively. From the results, the highest degradation efficiencies recorded for P-AKT-1 %, P-AKT-2 % and P-AKT-3 % were 90.5 %, 94.7 % and 90.2 % respectively. On the other hand, P-AKT-4 % and P-AKT-5 % have efficiencies of 84.5 % and 76.3 %.

These results exhibit higher efficiency when compared with the results reported by Gilja et al. [53] with a value of 77 % at 30 mg/L dosages and at 90 min and Jumat et al. [54] having higher efficiency of 96 % at a higher time frame of 300 min using solar irradiation. The rapid degradation can be ascribed to the action of the mediation of Fenton reagents. However, the photocatalytic activity of catalysts under irradiation with solar photons depends on vital parameters such as composition, crystallinity, crystallite size, and surface area [63]. However, the driving force for rapid photocatalysis is the incorporation of a Fenton reagent involving the reaction of H_2O_2 with the ferric ion from $FeCl_3$. These generate hydroxide radicals which combine with the radicals at the surface of the photocatalyst thereby enriching the system with required radical species for spontaneous dye degradation. Also, the appreciable elevated working temperature of the environment revealed in Fig. 6(e) supports the rapid degradation of the dye molecules in effluent. This is because, increase in temperature enhances the generation of more energy which consequently increases the activation energy of the system. This salvage the challenges of lower efficiency and high irradiation time for solar powered irradiation [64]. Furthermore, Tunc Dede et al. [58] pointed out the surface homogenizing propensity of Fenton reagents which aids dye-catalyst interaction. Hence, during solar photon irradiation, the π-π transitions in the polymeric chain alongside the excitation of the activated semiconductor induce the generation of singlet and triplet species. This leads to self-degradation of the dye molecules [65]. The formed species are characterized by high energy and react with oxygen and water molecules in the effluent to form peroxide, superoxide, and hydroxyl radicals [23]. Also, from the result, the lowest irradiation efficiency recorded for P-AKT-5 % may be attributed to higher loading of activated TiO_2—Nps which agglomerate to the surface as revealed from the SEM image in Fig. 2 (g-g[1]).

c. Effect of pH

Fig. 7(b)-(b[1]) revealed the effect of the pH on the degradation rates and quantity absorbed at equilibrium respectively. From the result, the optimal pH recorded for the photocatalytic process was at a slightly acidic pH of 5 and neutral pH (7). From the result, the least degradation performance recorded was for P-AKT-5 % at an acidic pH of 3 (25.4 %) while both P-AKT-1 % and P-AKT-5 % have a value of 32.3 % and 43 % respectively at an alkaline pH of 11. However, the pH value with the most effective degradation performance was at 5 and 7 with the highest record in P-AKT-2 % (94 % and 90 %) and P-AKT-3 (91 % and 85 %). The lowest performance of the photocatalyst was equally recorded by Gilja et al. [53] at pH 3 which is suggestive that a highly acidic medium lowers the adsorption performance of the nanocomposite photocatalyst [66]. Also, Babuponnusami et al. [67] added that Fenton processes are most efficient at the acidic range pH 4 while at higher pH range the Fe^{2+} is inactive at higher pH levels. From the result, the quantity of dye molecules adsorbed decreased as the pH values tended towards the acidic region. However, it increases with increasing pH up to the neutral point before the decrease sets in. This is because positive charges are built up by PANI due to its side amine groups' protonation along the polymeric chain. This coupled with amphoteric TiO_2—Nps forms an effective electrostatic bond with the anionic model dye (methylene blue) and decreases steadily due to gradual loss of positively charged groups [26,68]. Also, the decrease at higher pH is based on the generation of negatively charged groups due to deprotonation thereby creating stronger electrostatic repulsion with anionic dye molecules [69]. Additionally, studies have shown that the pH of the solution generally affects the surface charge of the photocatalyst nanocomposites, thereby influencing their degradation efficiencies. Mendre et al. [33] found that the pH of the solution had a significant impact. This impact is seen in the electrostatic interactions between the photocatalyst surface, solvent molecules, substrate, and charged radicals produced during photocatalytic oxidation.

d. Effect of Dosage

The effect of photocatalyst dosage on the degradation efficiency and quantity of the dye molecule absorbed is depicted in Fig. 8(a)-(a[1]). The result indicated the optimum catalyst dosage of 20 mg/L at a pH of 5. The highest degradation efficiency was 91.03 %, 94.45 %, 94.76 %, 73.74 % and 83.94 % for P-AKT-1 % to 5 % respectively. From Fig 8(a), the efficiency of each catalyst nanocomposite tested maintains constancy from 20 mg to 50 mg of dosage (Fig 8a). This shows that the optimum catalyst dosage is at 20 mg and an equilibrium is established beyond which further addition of dosage does not improve the system efficiency. However, the respective reduction in efficiency at 73.85 % and 83.46 % for P-AKT-4 % and P-AKT-5 % may be due to the impediment of the incident solar photons due to high dosing. Also, this could be due to possible agglomeration of the nanomaterial based on the clustered surface area of the catalyst which is equally reflected in Fig. 8(a[1]) [40]. Generally, increasing dosage comes with an increasing amount of dye molecules adsorbed up to the point of equilibrium (constancy) beyond which desorption sets in [70].

This is based on clustered surface area (agglomeration) leading to the availability of limited binding sites which initiate the generation of radicals (hydroxyl and superoxide) before degradation reaction [71,72]. Oyetade et al. [36] added that the aggregation of the particles up to the point of adhesion to one another occurs during the agglomeration of photocatalysts in nano form (10^{-9}). This results in the formation of large amount of agglomerates due to their higher surface energy. Although incident UV irradiation is limited by high catalyst loading of TiO_2 particles, there is also a possibility of agglomeration due to clustered surface area [44,62]. Beyond the optimal catalyst dosage, reduction in the surface area sets in leading to limited efficiency in dye degradation decolorization effectiveness decreases, even though similar to the report by Hou et al. [24].

e. Effect of Concentration

The result in Fig. 8(b)-(b[1]) shows the effect of varying concentrations on the degradation efficiency and quantity of dye molecules absorbed. The result indicated the most significant efficiency at 10 mg/L for P-AKT-1 % to 5 % having efficiencies of 85 %, 95 %, 94 %, 73 %, and 83.36

% respectively. However, at higher concentration (40 mg/L) of dye molecules low degradation rates of 41.67 %, 37.40 %, 35.73 %, 29 % and 24 % was adduced to the photocatalyst with the increasing loading of TiO_2 Nps. This is due to an increase in the amount of dye molecules as against the limited hydroxyl radicals generated from the process needful to degrade the organic molecules [73]. The optimal dye concentration reported in this study is similar to the photocatalytic study reported by Jangid et al. [22] and Mpelane et al. [74]. However, Dutta et al. [75] pointed out that the reduction in the quantity absorbed from the study is due to the high coverage of the dye molecules leading to the oversaturation of the active sites of the nano photocatalyst. This significantly reduces dye–photocatalyst interaction and lowers the generation of free radicals needed to mineralize the organic dyes during photon irradiation from sunlight.

3.7. Reaction mechanism

The reaction mechanism of the process involves the absorption of the irradiated solar photons by the photocatalysts and the photolytic reaction of the Fenton reagents which generates radical species. This ruptures the chemical bond of the dye molecules as described in Fig. 9(b). Also, the availability of the conjugated organic part (quinoid) and –NH•+ in the conducting macromolecules used in composite fabrication improves proficient dispersibility, surface functionality and effective adsorption of dye molecules from the effluent [74]. These appreciable features are due to the imparted surface modification by PANI in the mix apart from the lowering of bandgap which is for photoactivity to solar photons. On the other hand, the activated TiO_2—Nps in the mix having a larger bandgap provides the means for effective charge separation which is needed to accomplish a reduction in electron-hole recombination [23].

$$H_2O_2 + h\nu \rightarrow 2HO\bullet \quad (6)$$

$$3FeCl_3 + H_2O \rightarrow Fe_2O_3 + HCl \quad (7)$$

$$Fe_2O_3 + h\nu \rightarrow Fe^{2+} + HO\bullet \quad (8)$$

$$Fe^{2+} \rightarrow Fe^{3+} \quad (9)$$

$$Fe^{3+} + H_2O_2 + h\nu \rightarrow Fe^{2+} + HO\bullet + H^+ \quad (10)$$

Thus, upon solar irradiation, the mechanism involves electron excitation from HOMO to LUMO creating electron-hole pair which often travels back to the HOMO for recombination [23,74]. However, the presence of larger bandgap semiconductor material (AK-TiO_2—Nps) receives photoelectrons returning into the vacant conduction bands instead of returning to the HOMO of PANI as shown in Fig 8. This provides effective charge separation while the mediation of the process with the Fenton reagent enriches the photocatalyst surface with a high amount of radical species. This directly attacks the dye molecules, opens the aromatic ring and terminates to CO_2 and H_2O known as dye photocatalytic degradation as revealed in Eq. (6)-(10). Thus, the electrostatic interaction at the dye-photocatalyst interface in slightly acidic conditions (pH=5) and radical enrichment with Fenton reagents account for the faster reaction rate and time.

3.8. Efficiency comparisons

Table 3 comparatively describes the efficiency of the polyaniline-based photocatalysts driven by solar irradiation for dye photocatalysis as compared to the current study. The present photocatalytic approach indicated the most proficient fabricated composites (P-AKT-2 % and P-AKT-3 %) have respective efficiency of 95 % and 94 % at 90 min using 10 mg/L concentration of methylene and 20 mg/100 mL of catalyst loading. This rapid efficiency within the lower time frame has never been reported before for solar irradiated photocatalytic dye degradation.

From the Table, the current approach shows faster degradation time with considerably lower photocatalyst dosage. This is attributed to the process mediation with the Fenton reagent which boosts the photocatalytic performance of the nanocomposites. The simultaneous use of these high-performance photocatalysts and the Fenton-mediated process enhance high photocatalyst sensitivity to solar energy illumination. The use of the solar-driven process for dye remediation is often considered an affordable and clean energy process with profound sustainability when compared to UV irradiation. Hence, this approach is valid for the rapid remediation of dye-laden textile effluent posing great prospects in tackling the challenges of environmental pollution.

3.9. Reusability of fabricated photocatalysts

Fig. 10 shows the result of the reusability tests conducted on the most proficient photocatalysts (P-AKT-2 % and P-AKT-3 %) for photocatalytic remediation of methylene blue dye in effluent. The photocatalyst recovered from the treatment process was vacuum-dried, rinsed in DI water, and utilized in the following cycles to assess its viability for usage commercially and practically. The treatability performance was accessed for the second, third, fourth, and fifth cycles, respectively.

The figure indicates the considerable performance of more than 70 % dye degradation for more than four runs for P-AKT-3 % and less than 70 % at the 4th cycle of use for P-AKT-3 %. Although, P-AKT-2 % indicates effective stability and reusability after the fourth run [23]. However, the observed reduction in efficiency of the latter photocatalyst (P-AKT-3 %) could be due to catalyst agglomeration or mostly leaching of TiO_2 nanoparticles from the PANI matrix into the effluent. This lowers the activity of the photocatalyst after its recovery and subsequent reuse [21,64]. However, studies reveal that the use of high-surface-area matrix such as carbon-based materials has the potential of lowering leaching rate and possible agglomeration of the catalyst active sites during use thereby enhancing catalyst stability during dye effluent photocatalysis [84–87].

4. Conclusion

The study reveals the possibility of proficient degradation of industrial azo dye using methylene blue as model dye under solar photoillumination and Fenton-mediated process using fabricated nanocomposite photocatalyst. From the study, it is possible to accomplish efficient dye photocatalysis (95 % and 94 %) at a lower irradiation time of 90 min using sunlight energy with a solar radiance range of 1061–744 W/m^2 and the working temperature (<40 °C). This process salvages the appreciable longer irradiation time required and the need for alternative use of green energy sources other than the commonly used UV irradiation. The report also provided the experimental condition optimal concentration of 10 mg/L, dosage of 20 mg/100 mL of effluent and slightly acidic pH of 5 coupled with the possibility of catalyst regeneration and reuse up to 4th run. It is necessary to add that the study revealed the possibility of agglomeration of the nanoparticle with respect to higher loading of activated TiO_2—Nps in the mix. However, the study suggests the economic prospect of using the methods and photocatalysts for the degradation of industrial recalcitrant dye molecules. Thus, the study unveils the possibility of confronting the environmental pollution of toxic industrial dyes using cost-effective nanocomposite catalyst using green energy to aid the Sustainable development goals of the use of affordable and clean energy; goal (7) to achieve goal (3) good health and well-being, goal (6) clean water; goal (13) climatic action goal (14) life below water, goal (15) life on land and cumulatively goal (11) involving sustainable cities and communities. Additionally, the energy required to drive the process (sunlight photon) is time-dependent and may be unstable due to various climatic conditions within a specified area. Thus, to extend the frontiers of this study, solar power harvesting and storage technique for driving dye effluent photocatalysis holds great prospect in energy sustainability. Also,

further studies on the determination of the iron content of the effluent after dye photocatalysis is pivotal to mitigate its high usage which is deleterious to aquatic life.

CRediT authorship contribution statement

Joshua Akinropo Oyetade: Writing – review & editing, Writing – original draft, Methodology, Formal analysis, Data curation, Conceptualization. **Revocatus Lazaro Machunda:** Writing – review & editing, Validation, Supervision, Project administration. **Askwar Hilonga:** Writing – review & editing, Validation, Supervision, Project administration.

Declaration of competing interest

The authors declare that they have no known competing financial interests or personal relationships that could have appeared to influence the work reported in this paper.

Data availability

Data will be made available on request.

Acknowledgments

This work was supported and funded by the Regional Scholarship for Innovation Fund (RSIF), a flagship program of the Partnership for Skills in Applied Sciences, Engineering and Technology (PASET).

References

[1] S. Madhav, A. Ahamad, P. Singh, P.K. Mishra, A review of textile industry: wet processing, environmental impacts, and effluent treatment methods, Environ. Qual. Manag. 27 (3) (2018) 31–41.
[2] S. Saxena, A.S.M. Raja, A. Arputharaj, Challenges in sustainable wet processing of textiles, Text. Cloth. Sustain. Sustain. Text. Chem. Process. (2017) 43–79.
[3] A. Abayomi, J. Jamiu, O. Joshua, U. Judith, A. Taiwo, F. Moyo, Preparation and performance evaluation of an active anti-bleeding solution for laundering multicoloured textile apparels, Chem. J. 5 (1) (2020) 1–14.
[4] J.T. Chacko, K. Subramaniam, Enzymatic degradation of azo dyes – a review, Int. J. Environmetal Sci. 1 (6) (2011) 1250–1260, https://doi.org/10.6088/ijes.00106020018.
[5] J.M. Bidu, B. van der Bruggen, M.J. Rwiza, K.N. Njau, Current status of textile wastewater management practices and effluent characteristics in Tanzania, Water Sci. Technol. 83 (10) (2021) 2363–2376, https://doi.org/10.2166/wst.2021.133.
[6] E.O. Dada, A.R. Akanni, M.O. Akinola, Comparative physicochemical and genotoxicity assessments of textile mill company effluent and local Tie-and-Dye textile wastewater, J. Appl. Sci. Environ. Manag. 21 (5) (2017) 877–882.
[7] J.A. Oyetade, R.L. Machunda, A. Hilonga, Photocatalytic degradation of AZO dyes in textile wastewater by polyaniline composite catalyst-a review, Sci. African (2022) e01305.
[8] J.A. Oyetade, R.L. Machunda, A. Hilonga, Investigation of functional performance of treatment systems for textile wastewater in selected textile industries in Tanzania, Water Sci. Technol. (2023).
[9] P.K. Singh, R.L. Singh, Bio-removal of Azo Dyes: a Review, Int. J. Appl. Sci. Biotechnol. 5 (2) (2017) 108–126, https://doi.org/10.3126/ijasbt.v5i2.16881.
[10] B.D.C. Ventura-camargo, M.A. Marin-morales, Azo Dyes: characterization and Toxicity– A Review, Text. Light Ind. Sci. Technol. (May 2013) 2013.
[11] J.M. Jabar, A.I. Ogunmokun, T.A.A. Taleat, Color and fastness properties of mordanted Bridelia ferruginea B dyed cellulosic fabric, Fash. Text. 7 (1) (2020) 1–13.
[12] R.I. Alsantali, et al., Miscellaneous azo dyes: a comprehensive review on recent advancements in biological and industrial applications, Dye. Pigment. 199 (2022) 110050.
[13] R.D. Saini, Textile organic dyes: polluting effects and elimination methods from textile waste water, Int. J. Chem. Eng. Res. 9 (1) (2017) 975–6442 [Online]. Available: http://www.ripublication.com.
[14] M. Ismail, et al., Pollution, toxicity and carcinogenicity of organic dyes and their catalytic bio-remediation, Curr. Pharm. Des. 25 (34) (2019) 3645–3663.
[15] A. Sahu, R. Dosi, C. Kwiatkowski, S. Schmal, J.C. Poler, Advanced polymeric nanocomposite membranes for water and wastewater treatment: a comprehensive review, Polymers (Basel) 15 (3) (2023) 540.
[16] S.C. Schmal, R. Dosi, A. Fessler, C. Kwiatkowski, A. Sahu, J.C. Poler, Green synthesis of cellulose graft copolymers for anion exchange water purification, Cellulose (2023) 1–15.
[17] H. Ali, A.M. Ismail, Fabrication of magnetic Fe3O4/Polypyrrole/carbon black nanocomposite for effective uptake of Congo red and methylene blue dye: adsorption investigation and mechanism, J. Polym. Environ. 31 (3) (2023) 976–998.
[18] T. Shindhal, et al., A critical review on advances in the practices and perspectives for the treatment of dye industry wastewater, Bioengineered 12 (1) (2021) 70–87, https://doi.org/10.1080/21655979.2020.1863034.
[19] T. Karthik, R. Rathinamoorthy, Recycling and reuse of textile effluent sludge. in Environmental Implications of Recycling and Recycled Products, Springer, 2015, pp. 213–258.
[20] S. Sarkar, A. Banerjee, U. Halder, R. Biswas, R. Bandopadhyay, Degradation of synthetic Azo dyes of textile industry: a sustainable approach using microbial enzymes, Water Conserv. Sci. Eng. 2 (4) (2017) 121–131, https://doi.org/10.1007/s41101-017-0031-5.
[21] T. Amakali, et al., Photocatalytic degradation of rhodamine B dye and hydrogen evolution by hydrothermally synthesized NaBh4—spiked zns nanostructures, Front. Chem. 10 (2022) 1–15, https://doi.org/10.3389/fchem.2022.835832. April.
[22] S. Saha, N. Chaudhary, A. Kumar, M. Khanuja, Polymeric nanostructures for photocatalytic dye degradation: polyaniline for photocatalysis, SN Appl. Sci. 2 (6) (2020) 1–10, https://doi.org/10.1007/s42452-020-2928-4.
[23] S. Shahabuddin, et al., Synthesis of 2D boron nitride doped polyaniline hybrid nanocomposites for photocatalytic degradation of carcinogenic dyes from aqueous solution, Arab. J. Chem. 11 (6) (2018) 1000–1016, https://doi.org/10.1016/j.arabjc.2018.05.004.
[24] N.K. Jangid, S. Jadoun, A. Yadav, M. Srivastava, N. Kaur, Polyaniline-TiO2-based photocatalysts for dyes degradation 78 (8) (2021).
[25] O. Koysuren, H.N. Koysuren, Photocatalytic activity of polyaniline/Fe-doped TiO2 composites by in situ polymerization method, J. Macromol. Sci. Part A 56 (3) (2019) 267–276.
[26] J.A. Oyetade, R.L. Machunda, A. Hilonga, RSC Advances Functional impacts of polyaniline in composite matrix of photocatalysts : an instrumental overview, RSC Adv 13 (2023) 15467–15489, https://doi.org/10.1039/D3RA01243C.
[27] E. Pajootan, M. Arami, M. Rahimdokht, Application of carbon nanotubes coated electrodes and immobilized TiO2 for dye degradation in a continuous photocatalytic-electro-Fenton process, Ind. Eng. Chem. Res. 53 (42) (2014) 16261–16269.
[28] A.M. Abeish, H.M. Ang, H. Znad, Role of ferric and ferrous ions in the enhancement of the heterogeneous solar photocatalytic degradation of combined mixture of chlorophenols, Water Sci. Technol. 72 (9) (2015) 1561–1568.
[29] M.E. Borges, M. Sierra, E. Cuevas, R.D. García, P. Esparza, Photocatalysis with solar energy: sunlight-responsive photocatalyst based on TiO2 loaded on a natural material for wastewater treatment, Sol. Energy 135 (2016) 527–535.
[30] C. Hou, B. Hu, J. Zhu, Photocatalytic degradation of methylene blue over TiO2 pretreated with varying concentrations of NaOH, Catalysts 8 (12) (2018) 575.
[31] O. Koysuren, H.N. Koysuren, Photocatalytic activity of polyaniline/Fe-doped TiO 2 composites by in situ polymerization method, J. Macromol. Sci. Part A Pure Appl. Chem. 56 (3) (2019) 267–276, https://doi.org/10.1080/10601325.2019.1565548.
[32] A.K. Mishra, Conducting Polymers: concepts and Applications, J. At. Mol. Condens. Nano Phys. 5 (2) (2018) 159–193, https://doi.org/10.26713/jamcnp.v5i2.842.
[33] A. Mir, A. Kumar, U. Riaz, A short review on the synthesis and advance applications of polyaniline hydrogels, RSC Adv 12 (30) (2022) 19122–19132.
[34] S. Zhou, J. Bai, K. Huang, X. Ye, Y. Peng, M. Lei, Consideration of photoactivity of TiO2 pigments via the photodegration of methyl orange under UV irradiation, Materials (Basel) 15 (17) (2022) 6044.
[35] M.A.H. Devadi, M. Krishna, H.N.N. Murthy, B.S. Sathyanarayana, Statistical optimization for photocatalytic degradation of methylene blue by Ag-TiO2 nanoparticles, Proced. Mater. Sci. 5 (2014) 612–621, https://doi.org/10.1016/j.mspro.2014.07.307.
[36] J.A. Oyetade, A. Hilonga, R.L. Machunda, Performance evaluation of in situ Fenton-mediated photocatalysis of industrial dye effluent with enhanced TiO2 nanoparticle, AQUA-Water Infrastructure, Ecosyst. Soc. (2023).
[37] J.A. Oyetade, A. Hilonga, and R.L. Machunda, "Performance evaluation of in situ Fenton-mediated photocatalysis of industrial dye ef fl uent with enhanced TiO 2 nanoparticle," vol. 72, no. 6, pp. 1025–1041, 2023, 10.2166/aqua.2023.027.
[38] A. Mostafaei, A. Zolriasatein, Synthesis and characterization of conducting polyaniline nanocomposites containing ZnO nanorods, Prog. Nat. Sci. Mater. Int. 22 (4) (2012) 273–280.
[39] F. Habtamu, S. Berhanu, T. Mender, Polyaniline Supported Ag-doped ZnO nanocomposite: synthesis, characterization, and kinetics study for photocatalytic degradation of malachite green, J. Chem. (2021) vol. 2021.
[40] S. Zarrin, F. Heshmatpour, Photocatalytic activity of TiO2/Nb2O5/PANI and TiO2/Nb2O5/RGO as new nanocomposites for degradation of organic pollutants, J. Hazard. Mater. 351 (2018) 147–159, https://doi.org/10.1016/j.jhazmat.2018.02.052.
[41] J. Ma, J. Dai, Y. Duan, J. Zhang, L. Qiang, J. Xue, Fabrication of PANI-TiO2/rGO hybrid composites for enhanced photocatalysis of pollutant removal and hydrogen production, Renew. Energy 156 (2020) 1008–1018, https://doi.org/10.1016/j.renene.2020.04.104.
[42] M.I. Khan, et al., Conductive polymers and their nanocomposites as adsorbents in environmental applications, Polymers (Basel) 13 (21) (2021), https://doi.org/10.3390/polym13213810.
[43] M. Beygisangchin, S.A. Rashid, S. Shafie, A.R. Sadrolhosseini, Polyaniline thin films — a review, Polymers (Basel) 13 (2021) 1–46.
[44] H.J. Kleebe, S. Lauterbach, M. Müller, Transmission electron microscopy (TEM), BUNSENMAGAZIN (2010) 168.

[45] M.C. Arias, et al., Removal of the methylene blue dye (MB) with catalysts of Au-TiO₂: kinetic and degradation pathway, Mod. Res. Catal. 10 (01) (2021) 1–14, https://doi.org/10.4236/mrc.2021.101001.
[46] S. Wahyuni, E.S. Kunarti, R.T. Swasono, I. Kartini, Characterization and photocatalytic activity of TiO2(rod)-SiO2-polyaniline nanocomposite, Indones. J. Chem. 18 (2) (2018) 321–330, https://doi.org/10.22146/ijc.22550.
[47] D.S. Lee, T.K. Liu, Preparation of TiO 2 sol using TiCl 4 as a precursor, J. Sol-Gel Sci. Technol. 25 (2002) 121–136.
[48] M.M. Karkare, Choice of precursor not affecting the size of anatase TiO2 nanoparticles but affecting morphology under broader view, Int. Nano Lett. 4 (3) (2014) 111.
[49] L. Yu, H. Ruan, Y. Zheng, D. Li, A facile solvothermal method to produce ZnS quantum dots-decorated graphene nanosheets with superior photoactivity, Nanotechnology 24 (37) (2013) 375601.
[50] K.S.W. Sing, Reporting physisorption data for gas/solid systems with special reference to the determination of surface area and porosity (Recommendations 1984), Pure Appl. Chem. 57 (4) (1985) 603–619.
[51] M. Thommes, et al., Physisorption of gases, with special reference to the evaluation of surface area and pore size distribution (IUPAC Technical Report), Pure Appl. Chem. 87 (9–10) (2015) 1051–1069.
[52] G. Carja, R. Nakamura, T. Aida, H. Niiyama, Textural properties of layered double hydroxides: effect of magnesium substitution by copper or iron, Microporous Mesoporous Mater 47 (2–3) (2001) 275–284.
[53] A. Mezni, et al., Facile synthesis of highly thermally stable TiO2 photocatalysts, New J. Chem. 41 (12) (2017) 5021–5027, https://doi.org/10.1039/c7nj00747g.
[54] A. Kumar, G. Pandey, Preparation and photocatalytic activity of tio2/ppy/go for the degradation of rose bengal and victoria blue dye in visible light in aqueous solution, Desalin. Water Treat. 114 (2018) 265–284, https://doi.org/10.5004/dwt.2018.22312. July 2018.
[55] C. Hou, W. Liu, J. Zhu, Synthesis of NaOH-modified TiOF2 and its enhanced visible light photocatalytic performance on RhB, Catalysts 7 (8) (2017) 243.
[56] H. Wang, G. Yi, M. Tan, X. Zu, H. Luo, X. Jiang, Initial reactant controlled synthesis of double layered TiO2 nanostructures and characterization of its spectra of absorption and photoluminescence, Mater. Lett. 148 (2015) 5–8.
[57] I.S. Martakov, M.A. Torlopov, V.I. Mikhaylov, E.F. Krivoshapkina, V.E. Silant'ev, P. V. Krivoshapkin, Interaction of cellulose nanocrystals with titanium dioxide and peculiarities of hybrid structures formation, J. Sol-Gel Sci. Technol. 88 (1) (2018) 13–21.
[58] H. Ahmadizadegan, Surface modification of TiO2 nanoparticles with biodegradable nanocellolose and synthesis of novel polyimide/cellulose/TiO2 membrane, J. Colloid Interface Sci. 491 (2017) 390.
[59] K.L. Bhowmik, K. Deb, A. Bera, R.K. Nath, B. Saha, Charge transport through polyaniline incorporated electrically conducting functional paper, J. Phys. Chem. C 120 (11) (2016) 5855–5860, https://doi.org/10.1021/acs.jpcc.5b08650.
[60] B. Abebe, H.C. Ananda Murthy, Y. Dessie, Synthesis and characterization of Ti–Fe oxide nanomaterials: adsorption–degradation of methyl orange dye," *Arab*, J. Sci. Eng. 45 (6) (2020) 4609–4620.
[61] Y.W. Chen, Y.H. Hsu, Effects of reaction temperature on the photocatalytic activity of TiO2 with Pd and Cu cocatalysts, Catalysts 11 (8) (2021) 966.
[62] N.A.M. Barakat, M.A. Kanjwal, I.S. Chronakis, H.Y. Kim, Influence of temperature on the photodegradation process using Ag-doped TiO2 nanostructures: negative impact with the nanofibers, J. Mol. Catal. A Chem. 366 (2013) 333–340.
[63] S. Phromma, T. Wutikhun, P. Kasamechonchung, T. Eksangsri, C. Sapcharoenkun, Effect of calcination temperature on photocatalytic activity of synthesized TiO2 nanoparticles via wet ball milling sol-gel method, Appl. Sci. 10 (3) (2020) 993.
[64] I. Groeneveld, M. Kanelli, F. Ariese, M.R. van Bommel, Parameters that affect the photodegradation of dyes and pigments in solution and on substrate–An overview, Dye. Pigment. (2022) 110999.
[65] E. Subramanian, S. Subbulakshmi, C. Murugan, Inter-relationship between nanostructures of conducting polyaniline and the photocatalytic methylene blue dye degradation efficiencies of its hybrid composites with anatase TiO2, Mater. Res. Bull. 51 (2014) 128–135.
[66] I.Y. Sapurina, M.A. Shishov, Oxidative polymerization of aniline: molecular synthesis of polyaniline and the formation of supramolecular structures, New Polym. Spec. Appl. 740 (7) (2012) 272.
[67] Y. Andrea, T. Pogrebnaya, B. Kichonge, Effect of industrial dust deposition on photovoltaic module performance: experimental measurements in the tropical region, Int. J. photoenergy 2019 (2019) 1–10.
[68] A.H. Majeed, et al., A review on polyaniline: synthesis, properties, nanocomposites, and electrochemical applications, Int. J. Polym. Sci. 2022 (2022).
[69] Y. Jiao, X. Zheng, Y. Chang, D. Li, X. Sun, X. Liu, Zein-derived peptides as nanocarriers to increase the water solubility and stability of lutein, Food Funct 9 (1) (2018) 117–123.
[70] A. Kumar, G. Pandey, A review on the factors affecting the photocatalytic degradation of hazardous materials, Mater. Sci. Eng. Int. J 1 (3) (2017) 1–10.
[71] K. Suttiponparnit, J. Jiang, M. Sahu, S. Suvachittanont, T. Charinpanitkul, P. Biswas, Role of surface area, primary particle size, and crystal phase on titanium dioxide nanoparticle dispersion properties, Nanoscale Res. Lett. 6 (1) (2011) 1–8, https://doi.org/10.1007/s11671-010-9772-1.
[72] M.H. Abdellah, S.A. Nosier, A.H. El-Shazly, A.A. Mubarak, Photocatalytic decolorization of methylene blue using TiO2/UV system enhanced by air sparging, Alexandria Eng. J. 57 (4) (2018) 3727–3735, https://doi.org/10.1016/j.aej.2018.07.018.
[73] A. Babuponnusami, K. Muthukumar, Degradation of phenol in aqueous solution by fenton, sono-fenton and sono-photo-fenton methods, Clean–Soil, Air, Water 39 (2) (2011) 142–147.
[74] V. Gilja, K. Novaković, J. Travas-Sejdic, Z. Hrnjak-Murgić, M.K. Roković, M. Žic, Stability and synergistic effect of polyaniline/TiO2 photocatalysts in degradation of Azo dye in wastewater, Nanomaterials 7 (12) (2017) 1–16, https://doi.org/10.3390/nano7120412.
[75] N.A. Jumat, P.S. Wai, J.J. Ching, W.J. Basirun, Synthesis of polyaniline-TiO2 nanocomposites and their application in photocatalytic degradation, Polym. Polym. Compos. 25 (7) (2017) 507–514.
[76] M. Faisal, M.A. Rashed, M.M. Abdullah, F.A. Harraz, M. Jalalah, M.S. Al-Assiri, Efficient hydrazine electrochemical sensor based on PANI doped mesoporous SrTiO3 nanocomposite modified glassy carbon electrode, J. Electroanal. Chem. 879 (2020) 114805.
[77] M. Mitra, K. Kargupta, S. Ganguly, S. Goswami, D. Banerjee, Facile synthesis and thermoelectric properties of aluminum doped zinc oxide/polyaniline (AZO/PANI) hybrid, Synth. Met. 228 (2017) 25–31, https://doi.org/10.1016/j.synthmet.2017.03.017. October.
[78] L. Andronic, L. Isac, C. Cazan, A. Enesca, Simultaneous adsorption and photocatalysis processes based on ternary tio2 –cux s–fly ash hetero-structures, Appl. Sci. 10 (22) (2020) 1–16, https://doi.org/10.3390/app10228070.
[79] S. Sharma, et al., Visibly active FeO/ZnO@ PANI magnetic nano-photocatalyst for the degradation of 3-aminophenol, Top. Catal. 63 (11) (2020) 1302–1313.
[80] S. Ameen, H.K. Seo, M.Shaheer Akhtar, H.S. Shin, Novel graphene/polyaniline nanocomposites and its photocatalytic activity toward the degradation of rose Bengal dye, Chem. Eng. J. 210 (2012) 220–228, https://doi.org/10.1016/j.cej.2012.08.035.
[81] F. Deng, L. Min, X. Luo, S. Wu, S. Luo, Visible-light photocatalytic degradation performances and thermal stability due to the synergetic effect of TiO2 with conductive copolymers of polyaniline and polypyrrole, Nanoscale 5 (18) (2013) 8703–8710, https://doi.org/10.1039/c3nr02502k.
[82] Y. Lin, et al., Highly efficient photocatalytic degradation of organic pollutants by PANI-modified TiO2 composite, J. Phys. Chem. C 116 (9) (2012) 5764–5772.
[83] Y. Jia, et al., Regeneration of large bone defects using mesoporous silica coated magnetic nanoparticles during distraction osteogenesis, Nanomed. Nanotechn., Biol. Med. 21 (2019) 102040.
[84] T.B. Gelaw and B.K. Sarojini, "Enhancing the performance and recyclability of polyaniline/TiO2 hybrid nanocomposite by immobilizing with zein/hydroxyethyl cellulose composites for removal of anionic dyes," 2021.
[85] A. Mpelane, D.M. Katwire, H.H. Mungondori, P. Nyamukamba, R.T. Taziwa, Application of novel c-tio2-cfa/pan photocatalytic membranes in the removal of textile dyes in wastewater, Catalysts 10 (8) (2020) 1–17, https://doi.org/10.3390/catal10080909.
[86] G. Rajesh, S. Akilandeswari, D. Govindarajan, K. Thirumalai, Enhancement of photocatalytic activity of ZrO2 nanoparticles by doping with Mg for UV light photocatalytic degradation of methyl violet and methyl blue dyes, J. Mater. Sci. Mater. Electron. 31 (5) (2020) 4058–4072, https://doi.org/10.1007/s10854-020-02953-3.
[87] P. Muñoz-Flores, P.S. Poon, C. Sepulveda, C.O. Ania, J. Matos, Photocatalytic performance of carbon-containing CuMo-based catalysts under sunlight illumination, Catalysts 12 (1) (2022) 46.